



OPEN

Facile and reproducible method of stabilizing Bi_2O_3 phases confined in nanocrystallites embedded in amorphous matrix

Tomasz K. Pietrzak¹✉, Agata Jarocka¹, Cezariusz Jastrzębski¹, Tomasz Płociński², Marek Wasiucione¹ & Jerzy E. Garbarczyk¹

Bismuth sesquioxide (Bi_2O_3) draws much attention due to wide variety of phases in which it exists depending on the temperature. Among them, δ phase is specially interesting because of its high oxide ion conductivity and prospects of applications as an electrolyte in fuel cells. Unfortunately, it is stable only in a narrow temperature range ca. 730–830 °C. Our group has developed a facile and reproducible two-stage method of stabilizing Bi_2O_3 crystalline phases confined in nanocrystallites embedded in amorphous matrix. In the first stage, glassy materials were obtained by a routine melt-quenching method: pure Bi_2O_3 powders were melted in porcelain crucibles and fast-cooled down to room temperature. In the second step, the materials were appropriately heat-treated to induce formation of crystallites of β , δ or γ Bi_2O_3 phases confined in a glassy matrix, depending on the process conditions. It was found out that the vitrification of the initial Bi_2O_3 and the subsequent nanocrystallization were unexpectedly possible due to the presence of some Al, and Si impurities from the crucibles. Systematic DTA, XRD, optical, Raman and SEM/EDS studies were carried out to investigate the influence of the syntheses processes and allowed us to determine conditions under which the particular phases appear and remain stable down to room temperature.

Bismuth sesquioxide (Bi_2O_3) draws much attention due to a wide variety of phases which it adopts depending on the temperature. Among them, the δ phase exhibits a record high conductivity reaching 1 Scm^{-1} at 750 °C. For this reason, it has been considered a leading candidate for a ceramic electrolyte in intermediate temperature solid oxide fuel cells (IT-SOFCs)^{1,2}. Unfortunately, this phase is only stable in a narrow temperature range ca. 730–830 °C³. Below 730 °C it transforms to metastable and poorly conducting β - or γ -phases³. The β phase has also drawn much scientific interest due to its valuable optical properties and prospective applications in photocatalysis. However, the main phase stable at room temperature is the monoclinic α phase. Many attempts have been made to retain the defective fluorite structure of δ - Bi_2O_3 to temperatures below 730 °C. Most of them have involved solid solutions of Bi_2O_3 with substantial fractions of selected oxides (e.g.^{4,5}). In fact, such polycrystalline materials presented the fluorite-like ordering even at room temperature, but their conductivity was disappointingly much lower than expected from a δ - Bi_2O_3 -like structure^{4,5}.

In the last decades, several articles have reported that it is possible to extend downwards the stability range of certain simple compounds high-temperature crystalline phases using a very different approach. One of the first articles on such an effect was published in 1991 by Tatsumisago et al. in Nature⁶. They reported that a very rapid cooling ($> 10^5 \text{ K/s}$) of silver borate glasses very rich in AgI led to the formation of composite glass-ceramic solids with nanosized crystallites of α -AgI evenly dispersed in the glassy matrix. The most surprising was the presence of the α -phase at room temperature, knowing that in a bulk form this phase is stable only above 147 °C. Funke et al. stated that this phenomenon was due to the confinement effects of nanocrystallites embedded in a glassy matrix⁷.

A strikingly similar situation was observed by our group in the case of bismuthate glasses⁸. It was observed that the annealing of (nearly) pure Bi_2O_3 glasses at a temperature slightly higher than their glass transition temperature T_g led to the formation of nanosized crystallites of a high-temperature δ - Bi_2O_3 phase confined inside the glassy matrix. The resulting materials, including δ - Bi_2O_3 crystalline grains, were stable at room temperature for

¹Faculty of Physics, Warsaw University of Technology, Koszykowa 75, 00-662 Warsaw, Poland. ²Faculty of Materials Science and Engineering, Warsaw University of Technology, Wołoska 141, 02-507 Warsaw, Poland. ✉email: tomasz.pietrzak@pw.edu.pl

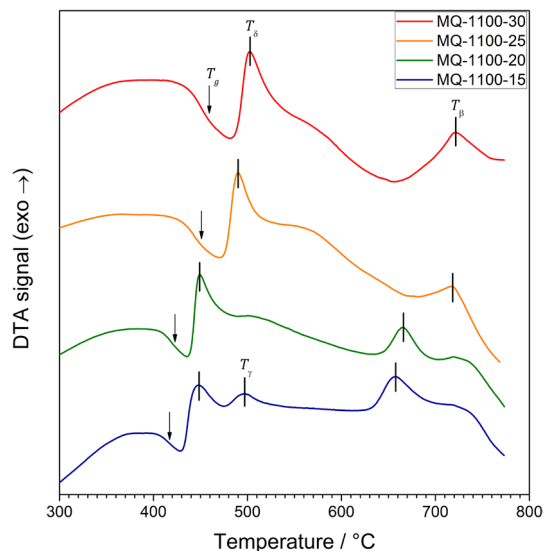


Figure 1. DTA traces of glassy samples synthesized under different conditions (melting time from 15 to 30 min at 1100 °C). Glass transition and crystallization thermal events are marked. The phases were ascribed to crystallization processes according to XRD results.

long periods of time (even over a year), despite the fact that the bulk δ - Bi_2O_3 is stable in the 730–830 °C range only³. Hence, an idea of a facile way to inexpensive and facile syntheses of bulk amounts of nanocrystallites of δ - Bi_2O_3 embedded in a residual glassy matrix arises. It consists of two stages only: (i) melting pure Bi_2O_3 in silica/alumina crucibles followed by their rapid quenching; (ii) heating the samples to ca 630 °C. Later, the same approach was used by Margha et al.⁹, who successfully synthesized glass ceramics of more complex Bi_2O_3 – BiFeO_3 system, containing the β and γ phases of Bi_2O_3 .

In both situations (α - AgI and δ - Bi_2O_3) there is no consistent and well-evidenced explanation of the mechanisms responsible for the stabilization of high temperature phases down to room temperature. Our hypothesis is that this phenomenon is due to the confinement of nanocrystallites of high-temperature phases in glassy matrices. This confinement does induce non-negligible interactions between the interiors of these crystallites, their surfaces, and the embedding glassy phase. These factors may cause a shift of local conditions acting on the nanosized crystallites of high-temperature phases, compared to those of the bulk phase. This shift may favor the stability of the high-temperature phase as long as it remains confined.

While the final explanation of the aforementioned mechanism still requires far fetched studies, in this work we attempted to identify experimental parameters that have a significant influence on phase stabilization in our bulk glass-nanoceramics. In comparison to the work reported in Ref.⁸, here we synthesized several samples with different melting times and extensively studied them by a range of methods, probing structure, thermal properties, microstructure, optical transitions and local ordering and dynamics: X-ray diffractometry (XRD), differential thermal analysis (DTA), scanning electron microscopy with energy dispersive spectroscopy (SEM/EDS), Raman spectroscopy and optical absorption measurements.

XRD studies allowed us to confirm the amorphousness of as-synthesized samples and identify the phases that appeared after heat treatment. The temperatures were correlated with the results of DTA measurements. SEM was used to investigate the microstructure of the samples and the elemental composition was determined with EDS. Micro-Raman spectroscopy can provide important information on the local structure in vitreous and ceramic materials. In this work, Raman spectroscopy was applied to probe the homogeneity of the samples and to detect the precipitation of other phases in the structure of Bi_2O_3 . Absorption spectroscopy provided information about the absorption edge in the material and hence helped to determine values of the optical gap.

Results

Differential thermal analyses (DTA). DTA traces of as-synthesized glasses are shown in Fig. 1. All glasses had been synthesized at 1100 °C. The batches differed in the melting time, which varied from 15 to 30 min (Table 1). Their DTA traces are typical for glassy materials. A step-like endothermic shift of the baseline, characteristic for glass transition, is followed by several exothermic peaks related to crystallization phenomena. One can see that the temperatures of these thermal events depend on the sample synthesis conditions. In general, the longer melting time, the higher these temperatures are. The temperature of glass transition (T_g) varies between 418 and 450 °C. The maximum of the main crystallization peak (T_δ) can be found in the range of 442–502 °C. All the temperatures are listed in the Table 2.

X-ray diffractometry (XRD). The diffraction patterns of the commercially purchased Bi_2O_3 reagent, which was used for all syntheses reported in this work, and the sample melted in a platinum crucible and subsequently rapidly cooled to room temperature are shown in Fig. 2a. It came not as a surprise that the starting

Sample ID	Melt. temp. (°C)	Melt. time	Al:Bi	Si:Bi
MQ-1100-15	1100	15	0.345	0.288
MQ-1100-20	1100	20	0.372	0.323
MQ-1100-25	1100	25	0.338	0.353
MQ-1100-30	1100	30	0.352	0.398

Table 1. List of the synthesized glassy samples with the process parameters (melting temperature and time) and the relative atomic content of Al and Si dopants.

Sample ID	T_g	T_δ	T_γ	T_β
MQ-1100-15	418	443	497	656
MQ-1100-20	419	448	–	665
MQ-1100-25	443	489	–	719
MQ-1100-30	450	502	–	719

Table 2. Temperatures of glass transition T_g and crystallizations (T_δ , T_γ , T_β) assigned to β , δ and γ - Bi_2O_3 phases. All values are given in °C.

reagent adopted the thermally stable α - Bi_2O_3 phase. The collected diffractogram was in good agreement with ICDD reference pattern no. 04-007-1342 (shown in the figure for comparison). The sample melted in a platinum crucible and subsequently quenched exhibited the same structure, i.e. α - Bi_2O_3 .

The patterns of the samples synthesized in porcelain crucibles are shown in Fig. 2b. Their shape is typical for amorphous materials. No distinct Bragg reflexes are present. On the contrary, two very broad and intensive halos centered at $2\Theta = 28.4^\circ$ and $2\Theta = 50.1^\circ$, respectively, are visible.

Room temperature XRD patterns of the samples that were heat-treated at $T_{max} = 630$ and 730°C are presented in Fig. 3a,b. One can clearly see that both glass synthesis conditions and temperatures T_{max} have impact on the crystalline phases emerging due to the heat-treatment at T_{max} . Three crystalline phases were identified: β (ICDD card no. 04-008-4464, tetragonal, space group P-421c), δ (ICDD card no. 04-015-0028, fcc, space group Pn-3m) and γ (ICDD card no. 04-007-2465, cubic, space group I23). The following samples contained pure δ - Bi_2O_3 phase: MQ-1100-20, MQ-1100-25 and MQ-1100-30—after heated to 630°C . Additionally, in some samples minor traces of hexagonal SiO_2 were found (ICDD card no. 01-075-3168). The phase composition of all studied samples is shown in Table 3.

Scanning electron microscopy (SEM) with energy dispersive X-ray spectroscopy (EDS). EDS analysis showed no impurities in the starting Bi_2O_3 powder, confirming its high purity, declared by the seller. The material consisted of microscopic grains. Typical sizes varied between 1 and $5\ \mu\text{m}$. Nevertheless, considerably bigger particles were also observed (Fig. 4a,b).

The structure of the crucibles used for syntheses was very interesting. Their inner part was porous. In our case, it means that it could be easily soaked with melted Bi_2O_3 . The external part of these crucibles was glazed, which ensured much lower porosity. Nevertheless, the elemental compositions (investigated with EDS) of both the interior and exterior parts of the crucible were the same: O—73%, Si—19.5%, Al—5.5%, Mg—1.1%, Na—0.9%. The relative uncertainties of this method were estimated as 3%.

Being aware of the effect of the crucibles on the glasses prepared in these crucibles, we have determined (by EDS) the elemental composition of all glassy samples under study. Besides the lines originating from Bi and O, the fingerprints of Si and Al were spotted in all the samples. Therefore, quantitative analyses were performed and the atomic contents of Bi, O, Al and Si were determined. The relative contents Al:Bi and Si:Al are shown in Fig. 5. One can see that the content of Al remains approximately constant, whereas the content of Si increases with the increasing time of melting during synthesis. While at this stage it is too early to propose any model describing this phenomenon, the experimental linear correlation between Si content in the batch and the melting time is quite obvious.

SEM images of selected representative glasses after their thermal treatment revealed considerably different microstructure (Figs. 6a–c). The samples containing the δ phase only consisted of small (ca. 10–20 nm) nanocrystallites uniformly distributed in the bulk sample. Noticeably larger grains (i.e. sub-micron) were observed in the samples, where the pure β phase was identified. On the contrary to the former samples, the sizes of grains of the γ phase in the latter sample exceeded $1\ \mu\text{m}$. A pronounced inhomogeneity was also observed in such cases (Fig. 6d).

Raman spectroscopy. Room temperature Raman spectra of as-synthesized glasses and the samples after an appropriate heat-treatment are shown in Fig. 7. The spectra of the glassy samples contain several broad maxima: below $200\ \text{cm}^{-1}$, around $400\ \text{cm}^{-1}$ and $620\ \text{cm}^{-1}$. The spectra of crystallized samples are more complex. In general, the samples originating from batches: MQ-1100-15 after heat-treatment at 630°C , and from MQ-1100-15 and MQ-1100-20 treated at 730°C contain several sharp lines, centered at 277, 328 and $538\ \text{cm}^{-1}$ (Fig. 7b,c).

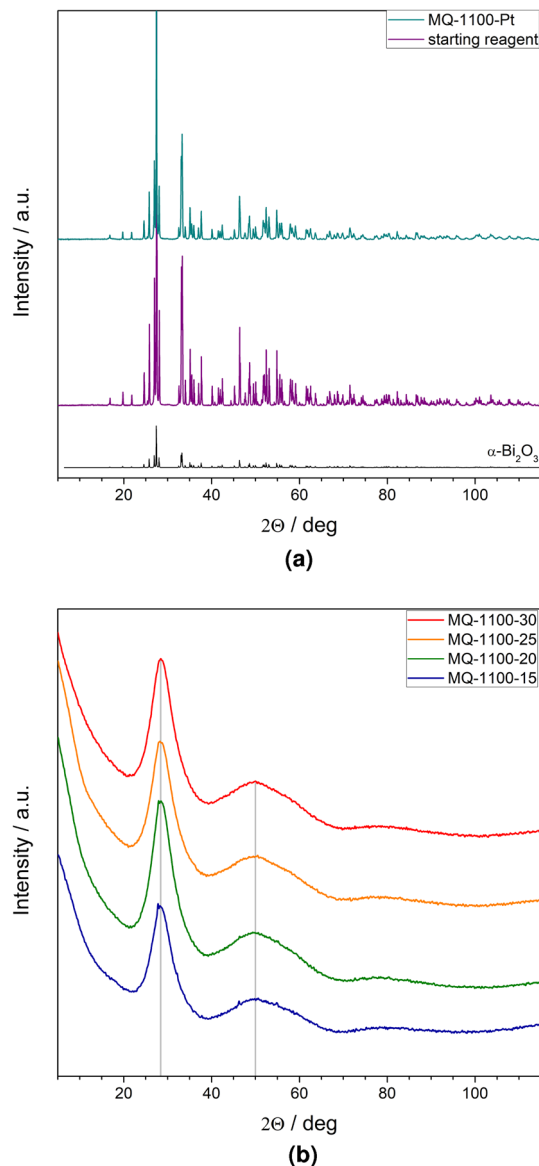
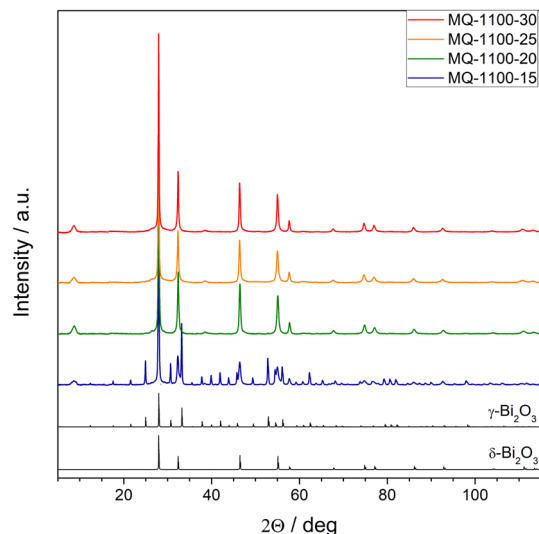


Figure 2. XRD patterns of: (a) starting Bi₂O₃ powder (reagent) and samples melt-quenched in a platinum crucible; α-Bi₂O₃ reference pattern is given in the bottom; (b) glassy samples processed in porcelain crucibles; distinctive amorphous *halos* are observed at $2\Theta = 28.4^\circ$ and $2\Theta = 50.1^\circ$.

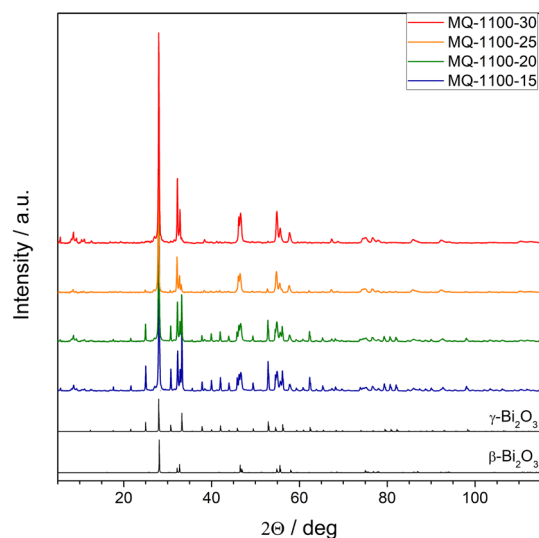
With the appearance of additional peaks, we observe the splitting of a wide peak located at about 130 cm^{-1} in the aforementioned samples. Crystallized samples originating from batches MQ-1100-20 and MQ-1100-25 and, especially, MQ-1100-30 exhibit either low intensity modes or no maxima at these Raman shifts. On the contrary, a broad maximum at 620 cm^{-1} is in this case more pronounced. This peak is partially overlapped for as-synthesized glasses by a wide band at about 400 cm^{-1} and only the right-side shoulder of this band at about 600 cm^{-1} is visible (Fig. 7a).

Optical characterization. In optical absorption measurements, the absorption edge for all studied glasses was within the visible range (Fig. 8a). Its shift towards lower wavelengths was observed with the increasing content of Si dopant (cf. Table 1). The first and second powers of the absorption coefficient $\alpha = \frac{1}{d} \ln \left(\frac{I_0}{I} \right)$ (where d is the thickness of the sample) were plotted versus $h\nu$ (Fig. 8b,c). Generally, for analysis and characterization of electronic absorption in solids within the UV-Vis-NIR, the most common is to represent the absorption coefficient as a function of energy or wavelength. Usually the dependency follows exponential relationship, where three main areas can be distinguished: (a) in higher energies—interband region (Tauc region), later on (b) Urbach edge region and in the lowest energies—charge transfer band defect states. Although, this dependence is much more defined for crystalline materials than for amorphous ones^{10,11}.

Absorption edge of amorphous semiconductors enables to define an optical gap and can be described by a power law^{11,12}. Mostly when it comes to glasses, one cannot determine if it is actual energy gap in states' density.



(a)



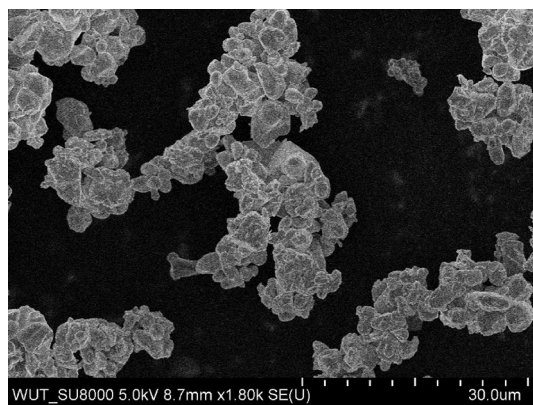
(b)

Figure 3. Room temperature XRD patterns of samples after their heat-treatment at 630 °C (top) and 730 °C (bottom). β , δ and γ - Bi_2O_3 reference patterns (ICDD cards no. 04-008-4464, 04-015-0028 and 04-007-2465, respectively) are given in the bottom.

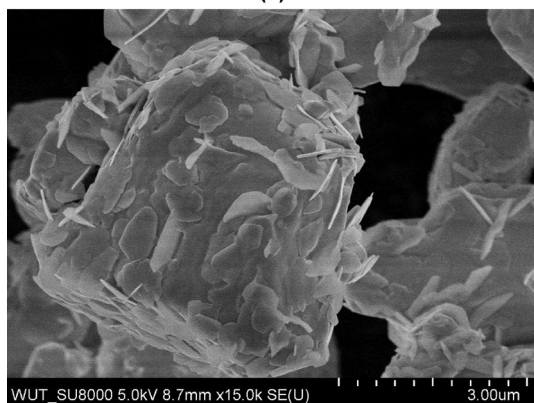
Sample ID	$T_{max} = 630\text{ }^\circ\text{C}$	$T_{max} = 730\text{ }^\circ\text{C}$
MQ-1100-15	γ (58 %) / δ (42 %)	γ (56 %) / β (46 %)
MQ-1100-20	δ	γ (49 %) / β (51 %)
MQ-1100-25	δ	β
MQ-1100-30	δ	β

Table 3. Phase composition (in vol percent) of the materials under study after their thermal treatment at $T_{max} = 630$ and $730\text{ }^\circ\text{C}$.

Therefore, it is more often considered as mobility gap (E_0) or just called optical gap or optical absorption edge^{12,13}. The linear parts of the curves were extrapolated to $\alpha = 0$ and hence the values of optical gap E_0 for each sample were estimated. From the $\alpha(h\nu)$ plot, the results are as follows: 2.58, 2.52, 2.42 and 2.58 eV for samples MQ-1100-15, 20, 25, and 30, respectively. The $\alpha^2(h\nu)$ coordinates yielded slightly different values: 2.69, 2.68, 2.61, 2.73 eV, respectively. There is no monotonic dependence of the optical band gap on the composition of the glasses.



(a)



(b)

Figure 4. SEM images acquired at different magnifications of the starting Bi_2O_3 powder used for all syntheses in this work. Two different parts of the reagent with various magnifications represent typical shapes of grains.

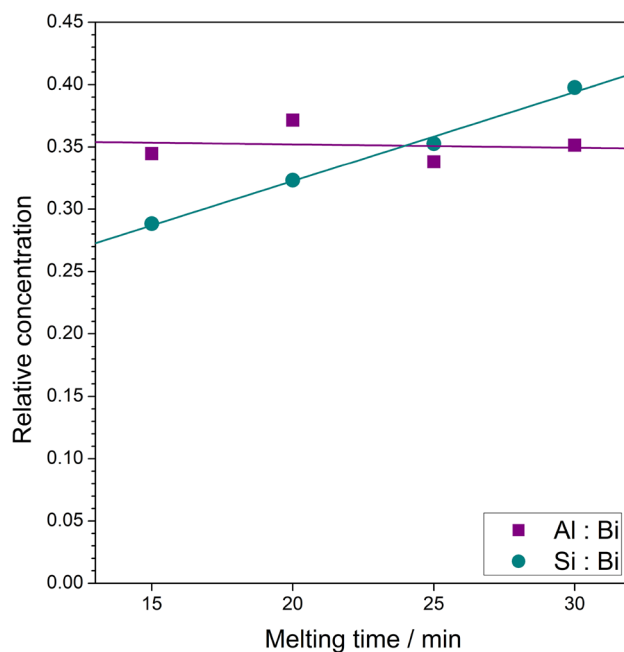


Figure 5. Relative concentrations of Si and Al dopants in the function of melting time during syntheses. Values are given as atomic Si:Bi and Al:Bi ratios and were determined from EDS analyses. Al content remains approximately constant regardless the melting time, while Si dopant linearly increases.

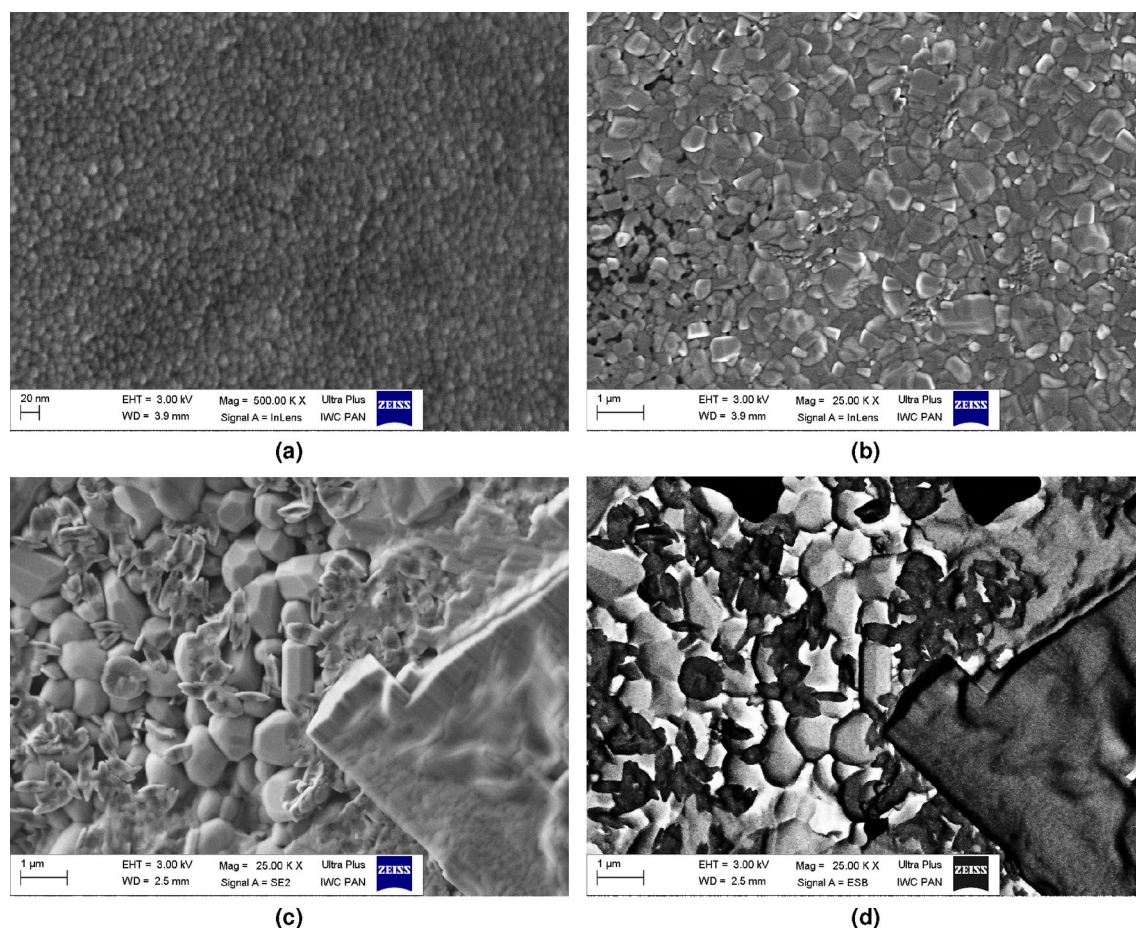


Figure 6. Representative SEM images of three phases—(a) δ – MQ-1100-30 heated up to 630 °C; (b) β – MQ-1100-30 heated up to 730 °C; (c,d) γ – MQ-1100-15 heated up to 730 °C—stabilized in glass-ceramics. One can see that average size of grains increases significantly from ca. 10–20 nm (for δ phase) to sub-micron (for γ phase). Differences in local compositions were pronounced only for the samples with the γ phase, as evidenced in electron backscattered mode (d).

Rather, we may assume that the values are scattered around 2.50 eV and 2.67 eV in the first (i.e. linear) and the second (i.e. $\alpha^2(h\nu)$) approach, respectively.

Discussion and conclusions

In this paper, we focused on numerous technological aspects of the syntheses of Bi_2O_3 glasses and their influence on the phenomenon of stabilization of different phases embedded in a glassy matrix. It was shown that the attempts to obtain glassy Bi_2O_3 with melt-quenching technique using Pt crucibles failed. The material without impurities/dopants crystallized in a monoclinic α structure, which is the stable low temperature phase in polycrystalline bismuth oxide.

Use of porcelain crucibles, composed mainly of SiO_2 and Al_2O_3 , resulted in significantly different outcomes. EDS experiments proved the solubility of these two oxides in melted bismuth oxide. The relative concentration of SiO_2 increased with the melting time, whereas the content of Al_2O_3 remained constant. The presence of these two glass formers / modifiers made it possible to obtain glassy samples in Bi_2O_3 – SiO_2 – Al_2O_3 ternary system. The glasses exhibited differences in glass transition and crystallization temperatures. Similar behavior was observed previously for V_2O_5 – P_2O_5 glasses synthesized with different time or temperatures¹⁴.

Very interesting results appeared when the glasses were heat-treated up to 630 and 730 °C. The synthesis conditions had a considerable influence on the phases that appeared in the samples. In general, the desirable δ phase was stabilized down to room temperature in samples heated up to 630 °C, whereas heating the samples to 730 °C resulted in stabilization of the β phase—another important for applications polymorph of Bi_2O_3 . The batches with short melting time created advantageous conditions for facile crystallization of the second phase—gamma.

Raman studies are extremely useful for identifying small amounts of another crystalline or amorphous phase in a given sample. This is very important in the case of materials exhibiting polymorphism¹⁵. In the case of Bi_2O_3 , the best known is its monoclinic α phase. The Raman spectrum of this phase contains many characteristic peaks¹⁶. In general, low-frequency peaks (i.e. below 200 cm^{-1}) are associated with the vibrations of Bi atoms, while those with frequencies above 200 cm^{-1} are the result of vibrations of oxygen atoms with respect to the Bi

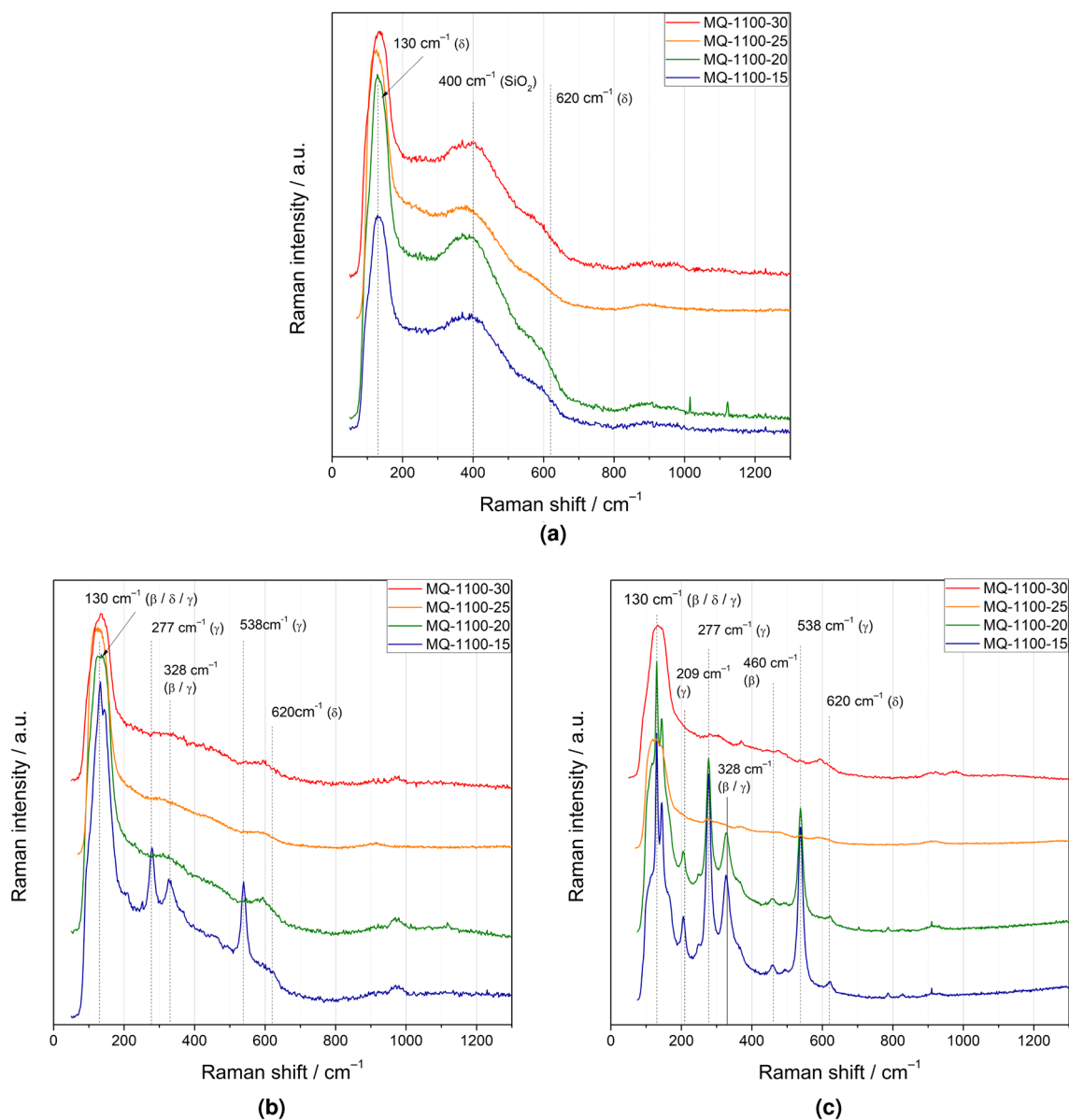


Figure 7. Room temperature Raman spectra of as-synthesized glasses (a) and the samples after heat-treatment at 630 °C (b) and 730 °C (c). The peaks have been tentatively assigned to various crystalline phases of Bi₂O₃.

atom causing Bi–O elongation or symmetric stretching of Bi–O–Bi bonds. In other phases of Bi₂O₃, also high-frequency vibrations (over 600 cm⁻¹) are observed.

Raman spectra of the Bi₂O₃ δ -phase has only one Raman active phonon of T_{g2} symmetry and thus one broad peak at 630 cm⁻¹ is reported^{17–20}. The β -Bi₂O₃ phase exhibits Raman bands at 125, 314, 376, and 460 cm⁻¹²¹. The Raman peaks at 144, 278, 320, 384, 450 and 550 cm⁻¹ are attributed to γ -Bi₂O₃^{22–24}. Moreover, in these Bi₂O₃ phases there are many other peaks of low intensity and their interpretation is ambiguous in literature.

Spectra presented in Fig. 7a have a characteristic broad peak at about 130 cm⁻¹, which is not due to selection rules for Raman scattering. Its presence and broadening is related to the defective structure of the δ phase. This cubic structure is related to the fluorite structure but has ordered defects in the oxygen sublattice in the 111 direction²⁵. Another reason of this broadening may be due to the atomic disorder resulting from the random orientation of the lone-pair orbitals of Bi atoms. Additionally, thermodynamic metastability of the δ -Bi₂O₃ phase at low temperature can lead to a phase transition or a partial decomposition of δ -Bi₂O₃ into another phase²⁶. The very wide peak at about 400 cm⁻¹ present in Fig. 7a–c may come from amorphous or glassy SiO₂ or SiO₂ with Al₂O₃ addition. The presence of Si and Al was confirmed for these samples in the SEM-EDS study. The Raman spectrum of vitreous silica is dominated by the region below 600 cm⁻¹. A major band occurs at 430 cm⁻¹. By adding Al₂O₃ to SiO₂, the intensity of this peak decreases, while the position practically does not change²⁷. Various disordered Al₂O₃ phases quite often show broad peaks at ca 400 cm⁻¹, as well as 900 cm⁻¹. A weak peak at about 900 cm⁻¹ is observed in practically all samples under study (Fig. 7a–c). The high intensity of the peak

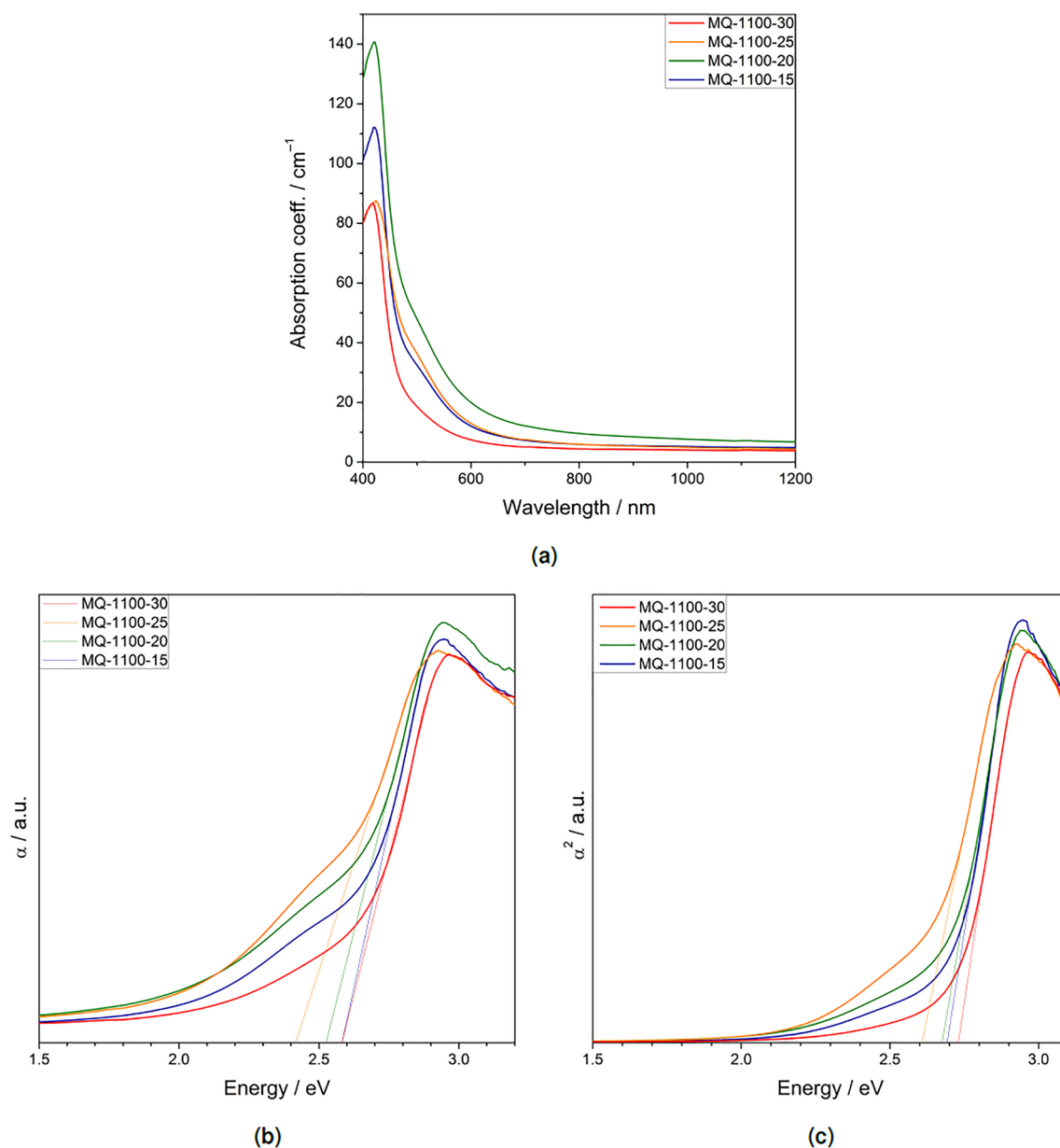


Figure 8. Absorption coefficient for synthesized glasses as a function of incident wavelength (a). Subsequently, the data were plotted in α vs. $h\nu$ (b) and α^2 vs. $h\nu$ (c) coordinates and normalized to determine the value of the optical gap.

around 400 cm^{-1} (Fig. 7a) may indicate that the SiO_2 and Al_2O_3 phases are located on the surface of the Bi_2O_3 crystalline nuclei.

When comparing the Raman spectra (Fig. 7) of the same samples with different heat-treatment, one can conclude as follows. Initially, all the as-synthesized glassy samples showed a δ phase (peak at 620 cm^{-1} and broad peak at 130 cm^{-1}) with addition of SiO_2 and/or Al_2O_3 (broad peak at 430 cm^{-1}) (Fig. 7a). Then, after heat-treatment at $630 \text{ }^\circ\text{C}$, a slight ordering of the δ phase can be seen (samples from MQ-1100-30, MQ-1100-25, and MQ-1100-20 batches (Fig. 7b). Additionally, in the case of the MQ-1100-15 batch the presence of the γ phase in the samples was observed (splitting of the peak at 130 cm^{-1} and the characteristic peak at 538 cm^{-1}).

Thermal treatment at even higher temperatures resulted in more distinct transition to the γ phase (batches MQ-1100-15, MQ-1100-20, Fig. 7c). In addition, the presence of the β phase in the samples from these batches (peak at about 460 cm^{-1}) and even small amounts of the δ phase (peak at about $600\text{--}620 \text{ cm}^{-1}$) is noticeable. As for the MQ-1100-30, and MQ-1100-25 batches, the dominance of the δ phase is visible. These conclusions largely coincide with the results obtained in X-ray studies (Table 3).

It was shown that the pristine glasses contain noticeable amounts of Al and Si dopants. Therefore, it was natural to think of these glasses as ternary $\text{Bi}_2\text{O}_3\text{--Al}_2\text{O}_3\text{--SiO}_2$ system. In terms of optical results, this approach meets some difficulties. The values of bismuth oxide optical gap reported in the literature vary strongly, usually from 2.0 to 3.96 eV^{28} . The exact value depends not only on the phase of Bi_2O_3 , but also on the preparation route

and the microstructure of the material (e.g. a thin film or polycrystalline ceramics)²⁹. The value mostly reported for bulk samples is 2.75–2.8 eV³⁰. Aluminum oxide and silicon oxide, regardless their exact structure, are well-known insulators. The reported values of the band gap for SiO₂, both crystalline (e.g. α -quartz) and amorphous, are around 9–10 eV^{31,32}. Bigger diversity is observed for aluminum oxide. For example, metastable θ -Al₂O₃ exhibits an indirect band gap of 4.64 eV³³, the stable α -Al₂O₃ exhibits a band gap of 7.6 eV³⁴ and amorphous alumina 7.0 eV³⁴. A gradual shift of the curves and hence, estimated absorption edge energies, was observed in Ref.³⁵ for binary Bi₂O₃–B₂O₃ glasses, where samples with higher concentration of boron oxide exhibited absorption edge in higher energies. In case of this study, there was no monotonic dependence of the optical band gap on the composition of the glasses. The values of the calculated optical band gap ranged from 2.42 to 2.73 eV, depending on the sample and the method of estimation. This is either because the Al and Si dopants did not affect significantly the mobility gap or the changes in concentrations were too small in this study to be reflected in the absorption measurements.

The Al and Si additives have a significant role in the whole process. Usually, δ -like phase of the fluorite structure is stabilized to lower temperature with expensive dopants of rare earth elements, e.g., Y³⁶, Yb³⁷, Dy and Tm³⁸, Th³⁹. Si and Al dopants were reported to stabilize β or γ phases only in polycrystalline forms^{40,41}. There is no evidence in the literature that these dopants may stabilize the δ phase by solid solution. Our studies have shown that the samples exhibited significantly different microstructure after crystallization. δ phase always existed in the form of small nanocrystallites embedded in a glassy matrix. Grains of the β phase were always larger and the γ phase appeared in micrometer-sized grains. It is an interesting observation that the position of the maximum in XRD patterns of glasses is similar to the (111) reflex of the δ phase or the (201) line of the β phase (approx. $2\Theta = 28^\circ$), rather than alpha ($2\Theta = 27.4^\circ$). It may suggest that the short-range order of glass resembles these two unstable phases rather than the stable monoclinic alpha. However, to verify this statement, other experiments will be scheduled, i.e. nuclear magnetic resonance (NMR) measurements and calculation of pair distribution function from a wide range XRD patterns collected with a silver lamp.

To conclude, in this work we have shown that Al and Si dopants tend to diffuse from porcelain crucibles to a Bi₂O₃ batch during its melting at 1100 °C. The concentration of Al was approximately the same, while the content of Si increased linearly with the increasing melting time (from 15 to 30 min). For even lower melting times, it was not possible to obtain a bismuthate glass using standard melt-quenching technique. In glasses heated to 630 °C, the nanocrystallites of the δ phase appeared, which remained stable after cooling down to room temperature. Similarly, the heating up to 730 °C resulted in appearance of a stable β phase. However, in samples with lower Si content, additional micrometric crystallites of the γ phase had a significant share.

While the exact role and position of Al and Si dopants in the structure has not been directly determined yet, our opinion is that the size and strain effects play the most dominant role in stabilization phenomenon. While Al/Si dopants facilitate the glass forming of bismuth oxide, the final stabilization is likely due to the confinement effects of nanocrystallites in the residual glassy matrix. The “power” of the size effect has already been proven by Dreyer et al.⁴², who synthesized stable free δ -Bi₂O₃ nanoparticles with minute dopant concentrations. Confinement effects in a glassy matrix (i.e. involving the local stress) could have an even stronger effect on δ -Bi₂O₃ stabilization, where no dopants would be necessary. Further experiments that could provide solid evidence for this phenomenon will be performed in the near future.

Methods

Commercial polycrystalline Bi₂O₃ (monoclinic α phase) powder (Arcos Organics, 99.9% extra pure) was put into porcelain VWR crucibles and subsequently inserted into a chamber furnace (manufacturer: Czylok, Poland) preheated to 1100 °C. The samples were kept in the furnace for 15–30 min (according to the description in Table 1) and then poured onto a stainless steel plate kept at room temperature and rapidly quenched with another plate. As a result, bulk transparent samples with orange tint and thickness ca 1 mm were obtained. As for reference, the same reagent was melted in a platinum crucible at 1100 °C for 30 min and cooled down accordingly.

Thermal analyses were performed using TA SDT Q600 apparatus from room temperature to 775 °C with the heating rate 10 °C/min. Ca. 10 mg of powdered glasses were put in alumina crucibles. The experiments were carried out in argon flow (100 ml/min).

Glassy samples were subject to further thermal treatment. Pieces of the glassy materials were put into 8 porcelain crucibles. First part was put into a chamber furnace LIFT 3 (manufacturer: Neoterm, Poland) and heated up to 630 °C, then kept 60 min at that temperature and cooled down to RT. The heating rate in this process was set to 1 °C/min, and the cooling rate was set to 3 °C/min. The procedure was performed in the air.

XRD studies of glasses and nanomaterials were carried out at room temperature in the air. A Malvern Panalytical Empyrean device was used with $K_{Cu\alpha}$ radiation and a nickel filter. The high-quality patterns were collected at a wide 2Θ range from 10° to 115° using PIXcel3D detector. The phase composition was analyzed using HighScore Plus software and PDF4 2021 database.

The surface topography investigations were performed by using Scanning Electron Microscope, Hitachi SU8000 (made in Naka, Japan) at the accelerating voltage of 5 kV. The low voltage was applied to reduce charging effect on uncoated samples. The observations were done by using SE and BSE electrons. At the same accelerating voltage the chemical composition analysis was performed by using EDS made by Thermo Fisher. The microstructure of the samples was also investigated with scanning electron microscopy (SEM) using Zeiss Ultra plus apparatus in the Institute of High Pressure Physics, Polish Academy of Sciences. For this experiment, a thin layer of carbon was sputtered on the surface of the samples.

The Raman spectra were measured with an inVia Renishaw spectrometer, utilizing either the 514 nm of an Ar laser or the 633 nm line of a He–Ne laser as sample excitation. Each Raman spectrum was collected for 30 s

(3 accumulations) at room temperature. Low laser beam powers were used to avoid the processes of structural degradation of the studied samples.

The absorption measurements were performed at room temperature using a Bentham PVE300 device equipped with a tunable light source (composed of xenon and halogen lamps), a monochromator, an integrating sphere and a silicon detector. Sample was placed between the integrating sphere and the light source. The light was directed at the sample using a set of mirrors. The procedure consisted of measuring the light intensity after it passes through the sample and dividing it by the incident light intensity. Therefore, the output value from this measurement was the transmission of the sample. Transmission is calculated into the absorption coefficient α using the following formulas: $T = \frac{I}{I_0}$, $\alpha = \frac{1}{d} \ln \left(\frac{1}{T} \right) = \frac{1}{d} \ln \left(\frac{I_0}{I} \right)$, where: T — transmission, I — light intensity after it passes through the sample, I_0 — incident light intensity, d — thickness of the sample.

Received: 18 June 2021; Accepted: 8 September 2021

Published online: 27 September 2021

References

- Wachsman, E. D. & Lee, K. T. Lowering the temperature of solid oxide fuel cells. *Science* **334**, 935–939 (2011).
- Basu, R. N. Materials for solid oxide fuel cells. In *Recent Trends in Fuel Cell Science and Technology* (ed. Basu, S.) 286–331 (Springer, 2007).
- Harwig, H. A. On the structure of Bismuth sesquioxide: The α , β , γ , and δ -phase. *Z. Anorg. Allg. Chem.* **444**, 151–166 (1978).
- Abrahams, I., Bush, A. J., Chan, S. C. M., Krok, F. & Wrobel, W. Stabilisation and characterisation of a new β III-phase in Zr-doped Bi_2O_3 . *J. Mater. Chem.* **11**, 1715–1721 (2001).
- Borowska-Centkowska, A. et al. Structure and conductivity in tungsten doped δ - Bi_2O_3 . *Solid State Ionics* **308**, 61–67 (2017).
- Tatsumisago, M., Shinkuma, Y. & Minami, T. Stabilization of superionic α -AgI at room temperature in a glass matrix. *Nature* **354**, 217–218 (1991).
- Funke, K. et al. Low-temperature α -AgI confined in glass: Structure and dynamics. *Solid State Ionics* **271**, 2–9 (2015).
- Pietrzak, T. K., Garbarczyk, J. E. & Wasiucione, M. Stabilization of superionic δ - Bi_2O_3 phase at room temperature by thermal nanocrystallization of bismuth oxide glasses. *Solid State Ionics* **323**, 78–84 (2018).
- Margha, F. H., Radwan, E. K., Badawy, M. I. & Gad-Allah, T. A. Bi_2O_3 - BiFeO_3 glass-ceramic: Controllable β - γ - Bi_2O_3 transformation and application as magnetic solar-driven photocatalyst for water decontamination. *ACS Omega* **5**, 14625–14634 (2020).
- Jha, A. *Inorganic Glasses for Photonics: Fundamentals, Engineering, and Applications* (Wiley, 2016).
- Elliott, S. R. *Physics of Amorphous Materials* (Longman, 1984).
- Mott, N. F. & Davis, E. A. *Electronic Processes in Non-crystalline Materials* (Oxford University Press, 2012).
- Varshneya, A. K. *Fundamentals of Inorganic Glasses* (Academic Press Inc, 1994).
- Pietrzak, T. K., Pawliszak, Ł., Michalski, P. P., Wasiucione, M. & Garbarczyk, J. E. Highly conductive $90\text{V}_2\text{O}_5 \cdot 10\text{P}_2\text{O}_5$ nanocrystalline cathode materials for lithium-ion batteries. *Procedia Eng.* **98**, 28–35 (2014).
- Depablos-Rivera, O., Martínez, A. & Rodil, S. E. Interpretation of the Raman spectra of bismuth oxide thin films presenting different crystallographic phases. *J. Alloys Compds.* **853**, 157245 (2021).
- Ardelean, I. & Rusu, D. Structural investigations of some Bi_2O_3 based glasses. *J. Optoelectron. Adv. Mater.* **10**(1), 66–73 (2008).
- Jiang, J., Lim, D. G., Ramadoss, K. & Ramanathan, S. Ionic conduction and unipolar resistance switching in δ -phase Bi_2O_3 thin films. *Solid State Electron.* **146**, 13–20 (2018).
- Skorodumova, N. V. et al. Random conductivity of δ - Bi_2O_3 films. *Appl. Phys. Lett.* **86**(24), 241910 (2005).
- Fang, H. T. et al. Optical properties of δ - Bi_2O_3 thin films grown by reactive sputtering. *Appl. Phys. Lett.* **87**, 231916 (2005).
- Díaz-Guerra, C., Almodóvar, P., Camacho-López, M., Camacho-López, S. & Piqueras, J. Formation of β - Bi_2O_3 and δ - Bi_2O_3 during laser irradiation of Bi films studied in-situ by spatially resolved Raman spectroscopy. *J. Alloy. Compd.* **723**, 520–526 (2017).
- Venugopalan, S. & Ramdas, A. K. Raman spectra of bismuth germanium oxide and bismuth silicon oxide. *Phys. Rev. B* **5**(10–15), 4065–4079 (1972).
- Yang, Y., Zhang, G., Yu, S. & Shen, X. Efficient removal of organic contaminants by a visible light driven photocatalyst $\text{Sr}_6\text{Bi}_2\text{O}_9$. *Chem. Eng. J.* **162**(1), 171–177 (2010).
- Moniz, Savio J. A., Blackman, Christopher S., Carmalt, Claire J. & Hyett, Geoffrey. MOCVD of crystalline extBi_2O_3 thin films using a single-source bismuth alkoxide precursor and their use in photodegradation of water. *J. Mater. Chem.* **20**, 7881–7886 (2010).
- Salazar-Pérez, A. J. et al. Structural evolution of extBi_2O_3 prepared by thermal oxidation of bismuth nano-particles. *Superficies y Vacío* **18**(3), 4–8 (2005).
- Keramidas, V. G. & White, W. B. Raman spectra of oxides with the fluorite structure. *J. Chem. Phys.* **59**, 1561 (1973).
- Fan, H. T., Pan, S. S., Teng, X. M., Ye, C. & Li, G. H. Structure and thermal stability of δ - Bi_2O_3 thin films deposited by reactive sputtering. *J. Phys. D Appl. Phys.* **39**, 1939–1943 (2006).
- Francis, McMillan Paul. & Bernard, Piriou. Raman spectroscopic studies of silicate and related glass structure: A review. *Bull. Minér.* **106**, 1–2 (1983).
- Leontie, L., Caraman, M., Visinoiu, A. & Rusu, G. I. On the optical properties of bismuth oxide thin films prepared by pulsed laser deposition. *Thin Solid Films* **473**, 230–235 (2005).
- Hayashi, K., Ishibashi, Y., Shimizu, T., Asahi, T. & Saitoh, A. Correlation with one- and two-photon absorptions in Bi_2O_3 containing B_2O_3 and SiO_2 glasses with zero photoelastic constant. *Appl. Phys. Express* **12**, 102010 (2019).
- Jabeen Fatima, M. J., Navaneeth, A. & Sindhu, S. Improved carrier mobility and bandgap tuning of zinc doped bismuth oxide. *RSC Adv.* **5**, 2504–2510 (2015).
- Tan, G. L., Lemon, M. F. & French, R. H. Optical properties and London dispersion forces of amorphous silica determined by vacuum ultraviolet spectroscopy and spectroscopic ellipsometry. *J. Am. Ceram. Soc.* **86**(11), 1885–92 (2003).
- Astasauskas, V. et al. Optical and electronic properties of amorphous silicon dioxide by single and double electron spectroscopy. *J. Electron. Spectrosc. Relat. Phenom.* **241**, 146829 (2020).
- Mo, Sh. D. & Ching, W. Y. Electronic and optical properties of θ - Al_2O_3 and comparison to α - Al_2O_3 . *Phys. Rev. B* **57**, 15219 (1998).
- Filatova, E. O. & Konashuk, A. S. Interpretation of the changing the band gap of Al_2O_3 depending on its crystalline form: Connection with different local symmetries. *J. Phys. Chem. C* **119**(35), 20755–20761 (2015).
- Watanabe, Y. et al. Two-photon absorption in binary Bi_2O_3 - B_2O_3 glass at 532 nm. *J. Non-Cryst. Solids* **240**, 212–220 (1998).
- Borowska-Centkowska, A. et al. Stability of tungsten-doped δ - Bi_3YO_6 . *Solid State Ionics* **345**, 115173 (2020).
- Leszczynska, M. et al. Thermal variation of structure and electrical conductivity in extBi_4 , $\text{extYbO}_{7.5}$. *Chem. Mater.* **25**(3), 326–336 (2013).
- Kiş, M., Polat, Y., Erdoğan, B. & Arı, M. New fabricated electrolytes based on Dy^{3+} - Tm^{3+} double-doped δ - Bi_2O_3 -type cubic phase. *J. Aust. Ceram. Soc.* **56**, 987–993 (2020).
- Sethi, A., Pandey, J., Uma, S. & Nagarajan, R. Luminescence properties of Eu^{3+} - and Tb^{3+} -doped δ - Bi_2O_3 stabilized by Th^{4+} substitution. *J. Am. Ceram. Soc.* **103**, 1027–1036 (2020).

40. Valant, M. & Suvorov, D. A stoichiometric model for sillenites. *Chem. Mater.* **14**(8), 3471–3476 (2002).
41. Weber, M., Rodriguez, R. D., Zahn, D. R. T. & Mehring, M. γ -Bi₂ O₃—To be or not to be? comparison of the sillenite γ -Bi₂ O₃ and Isomorphous Sillenite-Type Bi₁₂ SiO₂₀. *Inorg. Chem.* **57**(14), 8540–8549 (2018).
42. Dreyer, J. A. H. *et al.* Decrease of the required dopant concentration for δ -Bi₂ O₃ crystal stabilization through thermal quenching during single-step flame spray pyrolysis. *Cryst. Eng. Commun.* **18**, 2046 (2016).

Acknowledgements

Studies were funded by Materials Technologies project granted by Warsaw University of Technology under the program Excellence Initiative: Research University (ID-UB) (POB TechMat-1). We are grateful to Mr. Adam Presz from the Institute of High Pressure Physics, Polish Academy of Sciences for providing us with SEM images of the crystallized samples, and to Dr. Marek Pawłowski from our faculty for his kind aid in optical measurements.

Author contributions

T.K.P. synthesized the samples, conducted DTA and XRD measurements, wrote the main part of the manuscript; A.J. carried out optical measurements and participated in writing the manuscript; C.J. performed Raman measurements and analyses; T.P. carried out EDS analyses; M.W. and J.E.G. participated in discussion and writing the manuscript. All authors reviewed the manuscript.

Competing interests

The authors declare no competing interests.

Additional information

Correspondence and requests for materials should be addressed to T.K.P.

Reprints and permissions information is available at www.nature.com/reprints.

Publisher's note Springer Nature remains neutral with regard to jurisdictional claims in published maps and institutional affiliations.



Open Access This article is licensed under a Creative Commons Attribution 4.0 International License, which permits use, sharing, adaptation, distribution and reproduction in any medium or format, as long as you give appropriate credit to the original author(s) and the source, provide a link to the Creative Commons licence, and indicate if changes were made. The images or other third party material in this article are included in the article's Creative Commons licence, unless indicated otherwise in a credit line to the material. If material is not included in the article's Creative Commons licence and your intended use is not permitted by statutory regulation or exceeds the permitted use, you will need to obtain permission directly from the copyright holder. To view a copy of this licence, visit <http://creativecommons.org/licenses/by/4.0/>.

© The Author(s) 2021